STUDY ON THE PROCESS OF INTRUSION FORMATION USING CRYSTALLINE FEM ANALYSIS

N. Osawa*, Y. Tomita* and K. Hashimoto*

A crystalline FEM code developed by the authors to analyze cyclic plastic deformation behavior during fatigue process is improved by reexamining a strain hardening rule and a time integration algorithm. Using the expanded code, the deformation behavior of f.c.c. single crystal under cyclic loading conditions is investigated. The code has been shown to successfully simulate the localization of plastic deformation and the generation of irreversible slip in the course of loading history. The proposed strain hardening model can be used for the analysis of intrusion formation.

INTRODUCTION

Intrusion can be considered to be the origin of fatigue cracks, and the accumulation of irreversible slip within PSBs is one of the microscopic mechanisms of intrusion formation. Therefore, in order to explain the process of crack formation, analytical simulation is one of the prospective methods. Using this, we examined the microscopic mechanisms of plastic strain localization and irreversible slip generation.

Crystalline FEM analysis is applicable to such investigation. Crystalline FEM theory first was established by Peirce et al. (1). The authors (2) expanded this theory in order to analyze cyclic plastic deformation behavior during fatigue process, and the code has been shown to successfully simulate localization of plastic deformation and the generation of irreversible slip in the course of loading history. However, it has also been found that the code still needs further improvement.

In this paper, a strain hardening rule and time integration algorithm are reexamined in order to improve the FEM code of reference (2). Using the expanded code, the non-uniform deformation behavior of f.c.c. single crystal under cyclic loading conditions is investigated.

* Department of Naval Architecture and Ocean Engineering, Osaka University, Japan

BASIC EQUATIONS

The constitutive equation used in our analysis is based on the rate-dependent crystalline plasticity theory developed by Peirce et al. (1). It gives the relation between the Kirchhoff stress rate $\dot{\boldsymbol{\tau}}$, the shear strain rate on the slip system (a), $\dot{\gamma}^{(a)}$ and the total rates of stretching and spin, $\mathbf{D}$ and $\boldsymbol{\Omega}$. From the constitutive equation, the rate of the resolved shear stress (R.S.S.) of slip system (a), $\dot{\tau}^{(a)}$ is given by $\mathbf{D}$ and $\dot{\gamma}^{(a)}$.

Peirce et al. used the power law form expression of the shear rate $\dot{\gamma}^{(a)}$ in reference (1). This expression is not be applicable to the analysis of cyclic deformation behavior because it does not describe the Bauschinger effects. It is a well-known experimental result that dislocation density remains constant after cyclic hardening is saturated. This leads to the following hypotheses; multiplication does not occur during dislocation movements (a), and/or dislocations multiplied during slips disappear when the loading cycle is reversed (b).

Hypothesis Part (a) forces us to introduce back stress of slip systems in order to consider the Bauschinger effects. This is because strain hardening is mainly caused by the long range stress field which accelerates the dislocation movement in the opposite direction. This is the hardening rule employed in reference (2). On the other hand, hypothesis Part (b) leads us to reset the flow stress to the initial value when the loading cycle is reversed in order to analyze the Bauschinger effects.

In this paper, the strain hardening rule derived from the Part (b) is used. It is given by

$$\dot{\gamma}^{(a)} = \dot{a}^{(a)}\,\mathrm{sgn}\left(\frac{\tau^{(a)}}{g^{(a)}}\right)\left|\frac{\tau^{(a)}}{g^{(a)}}\right|^{1/m-1} \quad ; \quad \dot{g}^{(a)} = \sum_{(b)} h_{ab}\left|\dot{\gamma}^{(b)}\right| \quad \text{.....(1)}$$

$$g^{(a)} = g^{(a)}\big|_{init} \text{ on the reversal of loadng cycle}$$

Here, $g^{(a)}$ corresponds to the flow stress in the rate independent formulation, $\dot{a}^{(a)}$ represents the corresponding reference rate of shearing, and the exponent $1/m$ characterizes the material rate sensitivity. The hardening moduli h_{ab} of Eq. (1) is given by Eq. (2)

$$h_{ab} = qh + (1-q)h\delta_{ab} \text{ .....(2)}$$

Here, the parameter q sets the level of latent hardening. Eqs. (1) and (2) are the hardening rule employed in this paper.

NUMERICAL METHOD

Boundary value problems in this theory can be solved using the finite element method. In the same manner as references (1) and (2), analysis is based on the Lagrangian formulation with the initial unstressed state taken as reference, and the convected coordinate formulation reviewed in Needleman (3) is adopted.

In references (1) and (2), the rate constitutive equation is implemented by the one step, explicit rate tangent modulus method. As the residual force is not generally

dispelled at any loading step, numerical solutions lose the accuracy due to errors accumulated at each loading step. A new calculation method is developed in this paper, by which the residual force is dispelled at every step. As in the tangent modulus method, the slip increment on slip system during time increment Δt is calculated by a linear interpolation of shear rates at time t and $t+\Delta t$. $\mathbf{D}$ in the expression of $\dot{\tau}^{(\alpha)}$ can be represented by the nodal displacement rate $\dot{U}^J$. Integrating the constitutive equation with respect to time, the above relations lead to a set of equations for Kirchhoff stress components $\bar{\tau}^{ij}$ and the nodal displacement U^J at t and $t+\Delta t$. Taking the first 'guess' of $\bar{\tau}^{ij}|_{t+\Delta t}$ and $U^J|_{t+\Delta t}$ as $\bar{\tau}^{ij}|_{t+\Delta t}=\bar{\tau}^{ij}|_t$ and $U^J|_{t+\Delta t}=U^J|_t$, a set of successive iterations for $\bar{\tau}^{ij}|_{t+\Delta t}$ and $U^J|_{t+\Delta t}$ can be derived by using the Newton-Raphson procedure. Another set of successive iterations can also be derived from the principle of virtual work at $t+\Delta t$. From these two sets, an explicit algorithm for the successive corrections of $U^J|_{t+\Delta t}$ can be derived.

RESULTS AND DISCUSSION

In this paper, cyclic plastic deformation behavior of a rectangular parallelepiped f.c.c. crystal, shown in Figure 1, is analyzed. In Figure 1, coordinates x, y, z are the longitudinal, horizontal, and vertical edges of the crystal. The ratio of initial length, x_0, y_0, z_0, is $24:8:4$. The finite element model employed here is composed of $24\times8\times4$ 8-node isoparametric solid elements. Because of initial imperfections, the width and height of the crystal are reduced about 1% at $x_0/5$ from the crystal's ends.

The elasticity of the crystal is taken as isotropic, and characterized by Young's modulus and Poisson's ratio, shown in Table 1. Material constants which characterize the plastic shear deformation are also listed in Table 1. h and q of Eq. (2) are set to be constant, $h \equiv 30.4\text{MPa}$ and $q=1.4$.

As shown in Figure 1, the rate of the end displacement is controlled during cyclic loading while both ends remain shear free. End displacement is controlled so that the nominal strain amplitude is 3100×10^{-6} and the nominal strain rate is $\pm10^{-4}(1/\text{s})$. The cyclic loading is fully-reversed tensile-compressive loading. We call the period from the beginning of the loading to the first maximum tensile loading "the 0th cycle", and the period from the i th maximum tensile loading to the $i+1$ th maximum tensile loading "the i th cycle". The number of loading cycles is 120, and the loading direction is set to $[\sqrt{1/6},\sqrt{1/6},\sqrt{1/3}]$.

Figure 2 shows the computed load vs displacement curve. Load is defined by dividing the sum of the longitudinal components of reaction forces by the cross section area of the perfect crystal in initial state. The curves of each loading cycle retrace almost the same course throughout loading history. Thus, the stable stress-strain hysteresis loop obtained by means of the developed strain hardening rule corresponds to the appearance of cyclic plastic deformation of commonly used materials.

The symbols $I1, I2, \cdots I8$ stand for the points located at the initial imperfections shown in Figure 1. From the beginning of the loading to the 8th cycle, stress centers on $I3, I4, I5$ and $I6$, and the distribution of equivalent stress $\bar{\sigma}$ is almost symmetric with respect to the xz plane which passes through the center of the model. The degree of stress concentration during tensile loading tends to be more intensive than that during compressive loading. From the 9th to the 70th cycle, stress concentration at $I1, I5, I4$ and $I8$ increases while that at $I3$ and $I6$ decreases, and the symmetry of the

distribution of $\bar{\sigma}$ with respect to the xz plane is lost. After that, stress distribution remains almost constant. Figure 3 shows the distribution of $\bar{\sigma}$ at the maximum compressive and tensile loading points of the 120th cycle.

The accumulated sum of slips Γ defined by Eq. (3) is employed as the parameter which indicates the amount of plastic deformation.

$$\Gamma = \int_{s=0}^{t} \sum_{a=1,12} \left| \dot{\gamma}^{(a)} \right| ds \quad \text{.....(3)}$$

In the same manner as stress distribution, Γ centers on $I3, I4, I5$ and $I6$ from the beginning of the loading to the 8th cycle. From the 9th to the 70th cycle, a concentration of plastic deformation lying between $I1, I5, I4$ and $I8$ gradually occurs. After that, the localization of Γ continues. Figure 4 shows the distribution of Γ at the maximum tensile loading points of the 10th and the 120th cycle.

$\Delta\Gamma_{half}$ at each measuring point is defined by the increment of Γ during a half cycle (the period from maximum tensile/compressive loading to maximum compressive/tensile loading). The degree of irreversible slip generation and plastic deformation localization can be judged by the time history of $\Delta\Gamma_{half}$. $\Delta\Gamma_{half}$ remains constant when reversible slip occurs, while it changes when irreversible slip occurs. $\Delta\Gamma_{half}$ increases when plastic deformation concentrates while $\Delta\Gamma_{half}$ decreases when it declines. Figure 5 shows the time history of $\Delta\Gamma_{half}$ at $I1, I2, I3$ and $I4$. In this figure, the ordinate represents the increment of Γ during the tensile loading of the i th cycle when the abscissa equals $i-1/2$, and during the compressive loading when the abscissa equals i. Figure 5 shows that the localization of plastic deformation pauses after rapid localization, and then resumes at the 20th cycle only to saturate after the 70th cycle. After that, the value of $\Delta\Gamma_{half}$ at $I1$ and $I4$, the points where plastic deformation localizes, fluctuates considerably. At these points, the same slip systems work, but the amount of slip is different for each direction. This means that cross slip does not occur, but irreversible slip caused by 'random-walk' slip is generated in this region.

For the above results obtained by employing hypothesis Part (b) model, the initial imperfections cause nonuniform residual plastic deformation. This makes the heterogeneity of stress distribution increase and the difference of slip deformation during tensile/compressive loading become greater. This, in turn, leads to the localization of Γ and the generation of irreversible slip, which causes intrusion formation. The same phenomenon is found in the results obtained by employing Part (a) model in reference (2). In this respect, both Part (a) and Part (b) strain hardening models can be used for the analysis of intrusion formation. However, there are some differences between the two models. Localization of Γ derived from using Part (a) begins much earlier than that from Part (b), and cross slip occurs often with Part (a) while it does not occur at all with Part (b). The reason for such differences is as follows. With hypothesis Part (a), the difference of slip deformation during tensile and compressive loading makes the deviation of back stress increase, and the maximum drive force (R.S.S. – back stress) during tensile/compressive loading decreases while it increases during compressive/tensile loading. This forces the onset of localization and irreversible slip to quicken. When the deviation of back stress continues to increase, the maximum drive force in tensile/compressive direction decreases with time until finally it does not exceed the flow stress. When this happens, there appear some slip systems which work during only compressive/tensile loading, that is, cross slip occurs. On the other hand, the difference of the drive forces caused by the deviation of back stress does not occur with Part (b), the

onset of localization and irreversible slip is delayed and no cross slip occurs. It is not yet clear which model is suitable to analyze intrusion formation.

SYMBOLS USED

$\mathbf{D}$, $\mathbf{\Omega}$ total rates of stretching and spin

$\Delta\Gamma_{half}$ increment of the accumulated sum of slips during a half step

$g^{(a)}$ flow stress of the slip system (a)

$\gamma^{(a)}$ shear strain of the slip system (a)

Γ accumulated sum of slips

h_{ab} , q latent hardening module, parameter which sets the level of latent hardening

$\boldsymbol{\tau}$, $\bar{\tau}^{ij}$ Kirchhoff stress tensor and its components

$\tau^{(a)}$ resolved shear stress of the slip system (a)

U^J nodal displacement

REFERENCES

(1) Peirce, D., Asaro, R.J. and Needleman, A., Acta metall. Vol.31, No.12, 1983, pp.1951-1976.

(2) Osawa, N., Tomita, Y., Hashimoto, K. and Hirose, K., Proc. of the 8th Int. Offshore and Polar Eng. Conf., 1998, now printing.

(3) Needleman, A. Brown University Report MRL E-134, 1981

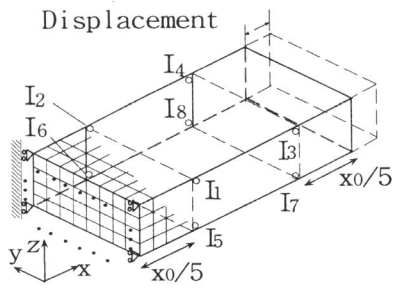

Figure 1 Finite element model for f.c.c. single crystal

TABLE 1- Material Properties used for calculation

Young's modulus	58800(MPa)
Poisson's Ratio	0.3
$\dot{a}^{(a)}$ of Eq. (1)	0.002
m of Eq. (1)	0.005
$g^{(a)}\|_{init}$ of Eq. (1)	58.8(MPa)

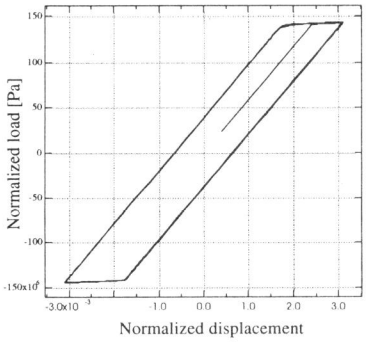

Figure 2 Normalized load vs displacement curve

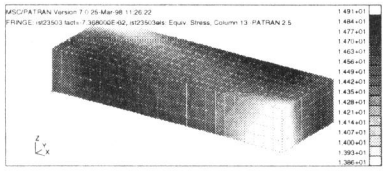

(a) At the maximum compressive loading point of the 120th cycle

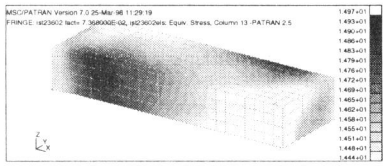

(b) At the maximum tensile loading point of the 120th cycle

Figure 3 Distribution of equivalent stress $\bar{\sigma}$

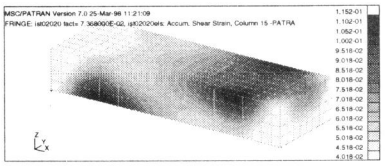

(a) At the maximum tensile loading point of the 10th cycle

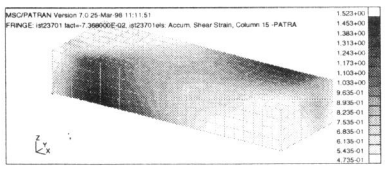

(b) At the maximum tensile loading point of the 120th cycle

Figure 4 Distribution of accumulated sum of slips Γ

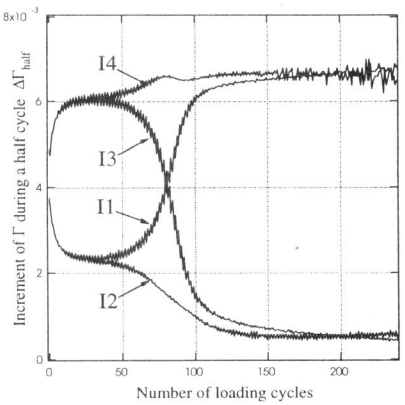

Figure 5 Time history of the increment of Γ during a half step $\Delta\Gamma_{half}$